Gallium Selenide Nanoribbons on Silicon Substrates for Photodetection

Pauline Hauchecorne, Farzan Gity, Mickael Martin, Hanako Okuno, Shubhadeep Bhattacharjee, Jérémy Moeyaert, Denis Rouchon, Bérangère Hyot, Paul Hurley, Thierry Baron

Gallium Selenide Nanoribbons on Silicon Substrates for Photodetection

Pauline Hauchecorne, Farzan Gity, Mickael Martin, Hanako Okuno, Shubhadeep Bhattacharjee, Jérémy Moeyaert, Denis Rouchon, Bérangère Hyot, Paul K. Hurley, and Thierry Baron*

ABSTRACT: Layered semiconductor gallium selenide (GaSe) is considered a potential candidate for optoelectronic applications because of its direct band gap. Monocrystalline material is, however, a prerequisite to fully exploit these properties in devices, where one-dimensional nano-objects could be considered as a model system. As a consequence of their large surface-to-volume ratio, nano-objects such as nanoribbons are interesting for photodetection applications. Here, we report the vapor–liquid– solid growth of GaSe nanoribbons by MOCVD on 300 mm silicon substrates. A growth model is proposed on the basis of a comprehensive study of the impact of the growth parameters on the nanoribbon morphology. The nanoribbon microstructure is investigated by HR-STEM and Raman spectroscopy characterizations. HR-STEM and TEM cross-sectional observations coupled with EDX analyses reveal a monocrystalline nanoribbon core covered with a native gallium-oxide shell. Test devices are made by contacting individual nanoribbon. The current versus voltage (I–V) characteristic obtained over a range of temperature (−50 to 100 °C) in the dark and under white light illumination is fitted on the basis of a back-to-back Schottky diode model. A stable and repeatable dynamic photoresponse is measured from the GaSe nanoribbons, with an ION/IOFF ratio of 17 at room temperature.

KEYWORDS: *2D materials, gallium selenide, GaSe, MOCVD, photodetectors, 300 mm, VLS growth*

INTRODUCTION

Photodetectors are optical sensors covering a wide range of wavelengths going from UV (0.2−0.4 μm) to IR (0.8−5 μm). UV photodetectors are mostly dedicated to gas and smoke detection, sanitary, environmental and health monitoring, radiation sensing, aerospace,[1−3] etc., whereas IR ones are used for autonomous vehicles, temperature monitoring, night vision, augmented reality, and biometrics.

In the development of photodetectors, there is a drive toward the use of nanostructured materials based on both scientific and environmental considerations. From the scientific perspective, the large surface-to-volume ratio of nanostructured materials increases the photoconductivity when compared to their bulk counterparts. In addition, the use of nanostructured sensors allows integration with microelectronic platforms for control, readout, and storage functions. From the environmental perspective, the semiconducting materials that comprise the photodetectors can contain critical and toxic materials, so the move to low volume nanostructures also supports the initiatives to minimize the use of raw materials in microelectronics technologies. All over the world, public organisms and scientific research groups report on the criticality of specific materials.[4−7] The European Union and the U.S. Geological Survey both published in 2020, evaluations of elements considered as critical for Europe and United States based on economy, industry, and target applications.[8,9] Apart from silicon imagers, most industrial photodetectors are based on Ga, In, P, Sb, Hg, Pb, and Ge, considered as critical materials. Finding substitutes or ways to reduce their use, while keeping an easy integration on microelectronic platforms, is key to developing more sustainable devices.

2D materials are potential candidates for optoelectronic applications, based on their large surface-to-volume ratio and the ability to tune electronic and optical properties through the number of 2D layers. Several demonstrators based on 2D materials for optoelectronic applications have already been developed.[10−16] Among them, transition metal dichalcogenide (TMDCs) semiconductors, such as MoS_2, have been demonstrated to display photodetection capabilities in the UV and visible ranges due to the direct bandgap of 1.8 eV for one monolayer.[17−19] Good responsivities and detectivities have

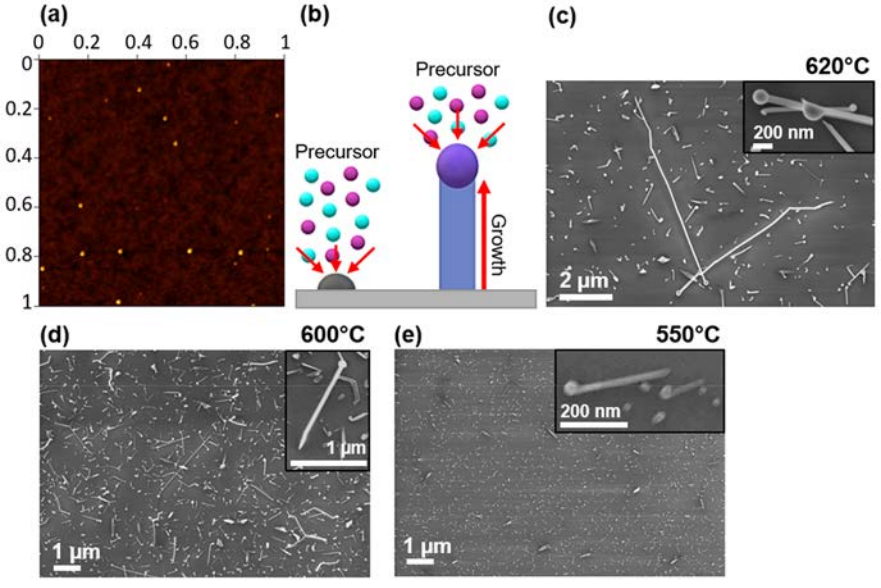

Figure 1. (a) AFM image of In droplets (scale: 1 × 1 μm^2). (b) Schematic illustrating the reaction occurring in the VLS growth mechanism in two times. First, the indium droplet (gray ball) is liquid, the substrate is solid, and the Ga and Se precursors (blue and purple balls, respectively) are gaseous. The precursors then react with the indium droplet, which leads to the growth of the NR. (c–e) SEM images of GaSe NRs after 50 s of growth time, at 620, 600, and 550 °C, respectively. Higher-magnification images of NRs are presented in the inset, showing the catalyst at the top end of NRs.

been obtained (1×10^5 A/W and 1×10^{14} Jones obtained by Han et al., 2018)[20] for a MoS_2 device with graphene contacts. But a major issue encountered by these devices is the long response time.[21] In addition, working with one monolayer leads to huge challenges on growth and large scale integration.

Another family of 2D materials, the post-transition metal monochalcogenide MXs (M = Ga or In; X = S, Se, or Te) or III–VI materials, present direct band gaps that are tunable through the number of layers.[22−24] The case of GaSe is of particular interest, as it is a direct bandgap semiconductor with an energy gap of around 2 eV in its bulk form.[25] In comparison with most 2D materials, the direct nature of the band gap appears for two monolayers and is kept for multilayers. Besides, the GaSe bandgap energy is fixed for a thickness superior at 15 monolayers.[24] On the other hand, other 2D materials such as TMDCs (MoS_2, WS_2, etc.) exhibit a direct bandgap only for one monolayer.[26] As a consequence, GaSe combines the advantages of 2D structures for detection within the visible spectrum, with an easier route to integration with conventional silicon integrated circuits. Several GaSe-based photodetectors have been demonstrated in the past years[22,23,27−32] and in 2020, Sorifi et al. and Tan et al. published very promising results showing responsivities of 2.6 and 3000 A/W and detectivities of 1×10^{12} Jones and 1×10^{13} Jones, at 380 and 405 nm, respectively.[33,34] Despite those first demonstrations, many challenges still have to be overcome to fabricate reliable devices, among them, the elaboration of single-crystal 2D materials on large scale using methods compatible with existing silicon technologies. An alternative to forming continuous 2D layers is to explore one-dimensional objects with good materials quality. However, the elaboration of these structures on large scale is also quite challenging.

The growth of 2D material-based nanowires and nanoribbons (NRs) has already been explored.[35−49] Different growth approaches have been studied and it is either possible to grow nano-objects with a relation of epitaxy with the substrate[41,46,47] or without, via different growth mechanisms such as vapor–liquid–solid or vapor–solid, for example. Among them, three groups have investigated the potential of GaSe one-dimensional objects for photodetection[38,40,43] revealing slow response time (on the order of some hundreds of milliseconds), potentially due to the existence of defects in the nanostructures creating charge traps. Most of these objects are grown by the vapor–liquid–solid (VLS) method, but no model currently exists to explain the different stages of the growth.

In this paper, we demonstrate the VLS growth of gallium selenide nanoribbons (GaSe-NRs) in an industrial MOCVD reactor, on 300 mm silicon substrates compatible with CMOS silicon platforms. The size and morphology of the NRs are tuned by controlling the growth parameters. An experimental-based model is proposed to explain the different growth steps of the GaSe NRs via the VLS method. The microstructure and chemical compositions of the NRs are studied by coupling HR-STEM and STEM/EDX analyses. Preliminary photodetection capabilities of the NRs are investigated via electrical characterization under illumination (white light), for different temperatures ranging from −50 to 100 °C.

EXPERIMENTAL SECTION

GaSe NR Growth. The GaSe NRs are grown by MOCVD in an Applied Materials reactor via the vapor solid liquid method on 300 mm Si(100) substrates covered by 100 nm of thermally grown silicon dioxide. In situ indium droplets formed in the MOCVD reactor, using trimetylindium $In(CH_3)_3$ (TMIn) as precursor, are used as catalyst [FR1913421]. After droplet formation, gallium and selenium precursors (trimethylgallium $Ga(CH_3)_3$ (TMGa)) and (diisopropylselenide $Se(C_3H_7)_2$ (DiPSe)), are introduced in the growth chamber to form GaSe NRs. The typical growth time is between 500 and 1000 s, and the growth temperature is between 500 and 650 °C. Hydrogen is used as carrier gas and the total pressure in the chamber is controlled between 5 and 20 Torr.

Raman Spectroscopy. The crystal quality of the NRs is investigated by Raman spectroscopy. Spectra are recorded in the

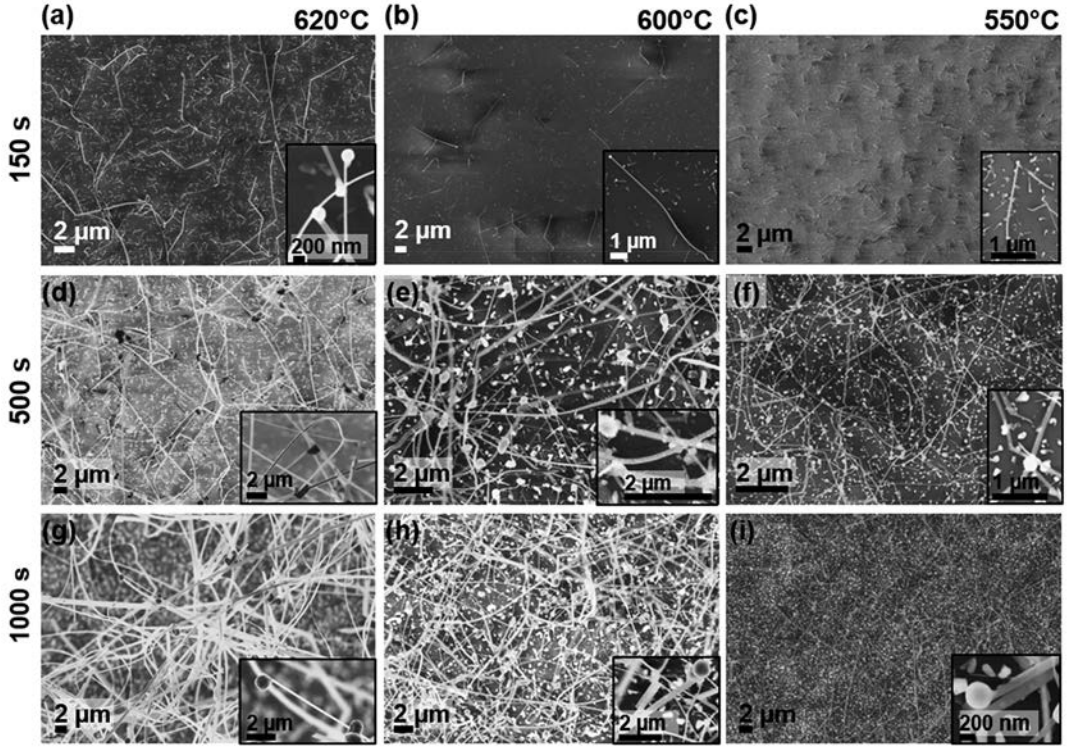

Figure 2. SEM images of GaSe NRs grown at 620, 600, and 550 °C, for 150, 500, and 1000 s. Higher-magnification images of NRs are presented in the insets. (a, d, g) Growth at 620 °C, (b, e, h) growth at 600 °C, and (c, f, (i) growth at 550 °C.

backscattering geometry using a Renishaw In-Via. The light is focused on the NRs surface using a 100× objective (09 numerical aperture), resulting in a spot diameter of around 0.8 μm. The excitation wavelength is 532 nm with a typical laser power of 1 mW.

Photoluminescence. Photoluminescence analyses are done in an automated μPL tool Horiba LabRAM HR with a 514 nm laser focused on the NRs via a 50× and a 100× objective.

SEM Characterization. SEM images were recorded with a Zeiss Ultra SEM equipment.

STEM Characterization. STEM imaging and energy dispersive X-ray spectroscopy (EDX) have been carried out using a Cs-corrected Thermo Fisher Themis at 200 kV. HAADF-STEM images were acquired using a convergence semiangle of 20 mrad and collecting scattering >55 mrad.

Sample Preparation and Electrical Characterization. Test devices are made by contacting individual NR. After the growth, NRs are removed from their original substrate by placing pieces of wafer in IPA solution, in an ultrasonic bath. The solution is then dropcasted onto a prepatterned (with e-beam lithography alignment markers) 90 nm SiO_2/p++ doped Si substrate. The substrate was gently rinsed with acetone/IPA solution (without sonication). Next, transfer length method (TLM) structures were defined using the Raith Pionner e-beam lithography system on individual GaSe NR. The channel length spacing of 0.5−4 μm and contact width of 0.4 μm were defined with an accelerating voltage of 20 kV and beam current of ∼220 pA. High-work-function electrodes (Ni (45 nm)/Au (45 nm)) were deposited using e-beam evaporation followed by lift-off of PMMA resist. DC and transient electrical characterization of the devices were performed in a dry-air microchamber Cascade Summit 12000 probe station using a B1500 semiconductor device analyzer (SDA). The light induced $I-V$ measurements were performed under microscope illumination of the probe station incandescent lamp (150 W).

RESULTS AND DISCUSSION

Figure 1a shows an AFM picture of indium (In) droplets formed onto 100 nm thick SiO_2 layer on Si(100) substrate. These droplets are deposited in situ in the MOCVD reactor by adjusting the temperature and the In flux and serve as catalysts for the subsequent GaSe growth. Typical deposition temperature and time are 400 °C and 90 s, respectively, which ensures trimethylindium (TMIn) decomposition at the surface of the substrate and formation of isolated droplets on the whole 300 mm wafer. Typical diameters of the In droplets ranged from 11 to 20 nm, with an average size of 15 nm and a density of 1×10^9 cm^{-2}, measured from AFM acquisition. Some previous studies have used gallium, gold, selenium, or silver droplets as catalysts for the growth of III−VI nanowires or NRs[36,37,39,44,48−51] (by CVD or in horizontal furnace). Here, we have chosen indium as it is compatible with our 300 mm MOCVD cluster tool.

After the formation of In droplets, the TMIn flux is stopped and the substrate is heated up to proceed to the GaSe NRs growth. Prior to the growth, we checked that this temperature increase does not modify the morphology and the density of the In droplets. The influence of growth time and temperature, and to a lesser extent of VI/III ratio, on the morphology of GaSe NRs have been studied. The growth temperature is kept above 500 °C and varied between 550 and 620 °C to ensure a good decomposition of the trimethylgallium (TMGa) and diisopropylselenide (DiPSe) precursors and to avoid carbon incorporation as much as possible. The molecular flows of the gallium (Ga) and selenium (Se) precursors, the total pressure, and the VI/III ratio are maintained constant at 63, 322 μmol/min, 20 Torr, and 5.1, respectively. The growth time is varied between 50 and 1000 s. A schematic summarizing the chemical reactions occurring during the VLS growth is presented in the Figure 1b.

Figure 1c−e shows SEM images of GaSe NRs after 50 s of growth for three different temperatures (620, 600, and 550

Table 1. NR Dimensions (in length and width) as a Function of the Growth Parameters (Growth Temperature and VI/III Ratios)[a]

			growth time			
growth temperature			50 s	150 s	500 s	1000 s
			VI/III ratio: 5.1			
620 °C	nanoribbons	width	80−100 nm	80−190 nm	220−370 nm	270−675 nm
		length	7−12 μm	tens of μm	tens of μm	tens of μm
600 °C	nanoribbons	width	60−70 nm	80−140 nm	100−250 nm	180−320 nm
		length	1.5−3 μm	6−11 μm	tens of μm	tens of μm
550 °C	nanoribbons	width	20−30 nm	40−60 nm	60−120 nm	80−150 nm
		length	0.2−0.3 μm	1−2.6 μm	tens of μm	tens of μm
			VI/III ratio: 4.2			
550 °C	nanoribbons	width	14 − 21 nm	20 − 36 nm	40−100 nm	76−150 nm
		length	0.1−0.2 μm	0.4−1.5 μm	2.5−12 μm	tens of μm

[a]The values are reported for VI/III ratio of 5.1 at 620, 600, and 550 °C and for VI/III ratio of 4.2 at 550 °C, for four growth times (50, 150, 500, and 1000 s). Minimum and maximum dimensions are indicated in each case. The growth conditions where the morphology of the NRs is controllable are indicated by the red zone.

Table 2. Catalysts Dimensions As a Function of the Growth Parameters (Growth Temperature and VI/III Ratios)[a]

		growth time			
growth temperatures	catalysts	50 s	150 s	500 s	1000 s
		VI/III ratio: 5.1			
620 °C	catalyst diameter	166−192 nm	200−430 nm	0.86−1.4 μm	1−2 μm
	nanoribbon widths	80−100 nm	80−190 nm	220−370 nm	270−675 nm
600 °C	catalyst diameter	80−120 nm	180−260 nm	340−700 nm	490−980 nm
	nanoribbon widths	60−70 nm	80−140 nm	100−250 nm	180−320 nm
550 °C	catalyst diameter	30−60 nm	60−90 nm	190−280 nm	280−420 nm
	nanoribbon widths	20−30 nm	40−60 nm	60−120 nm	80−150 nm
		VI/III ratio: 4.2			
550 °C	catalyst diameter	20−35 nm	60−80 nm	170−230 nm	340−450 nm
	nanoribbon widths	14−21 nm	20−36 nm	40−100 nm	76−150 nm

[a]The values are reported for VI/III ratio of 5.1 at 620, 600, and 550°C and for VI/III of 4.2 at 550°C, for four growth times (50, 150, 500, and 1000 s). Minimum and maximum dimensions are indicated in each case.

°C). We observe the presence of two populations of NRs that could reveal different growth mechanisms. Here, we only focus on the longer-grown NRs observed. As temperature decreases, the difference in length between NRs decreases accordingly. In both cases, we observe the presence of catalysts at the top of NRs (shown in the insets).

Figure 2 shows SEM images of NRs at different growth times ranging from 150 to 1000 s, for the three studied temperatures. The typical dimensions of the NRs are provided in Table 1, for four growth times (50, 150, 500, and 1000 s). All the indicated values are based on SEM image analyses with statistical measurements based on a population of about 10−20 NRs. The results indicate clearly a dependence of the NR length and width on temperature and growth time. The longest and largest NRs are obtained at 620 °C and 1000 s, whereas the smallest and thinnest are obtained at 550 °C and 50 s. A large dispersion in width is observed at 620 °C (1000 s) but this size dispersion decreases accordingly, as the growth temperature is reduced. The SEM images show as well that the catalysts are still present regardless the investigated growth conditions and temperatures.

At 620 °C, controlling NRs dimensions is quite challenging, but below 620 °C and for short growth times (less than 200 s), the growth rates can be estimated. Statistical measurements are made again on a population of about 10−20 NRs, at the center of the wafer. The error value is calculated using the standard deviation formula. All the calculated growth rates and errors are presented in the table from the Figure S1. At 600 °C, high growth rates are observed between 42 and 59 nm/s, estimated for 50 and 150 s grown nanostructures. At 550 °C, the growth rates range between 6 and 13 nm/s, estimated from 50 to 200 s grown nanostructures. Therefore, 550 °C appears to be the optimum temperature to control NR growth and dimensions. To complete this parametric study, we have investigated the influence of the VI/III ratio on the NR morphology, at a constant temperature of 550 °C.

In addition to the VI/III ratio of 5.1, two other ratios have been studied, one with an addition of selenium (VI/III: 5.9) and another one with a reduction of selenium (VI/III: 4.2). Only the VI/III ratio of 5.9 leads to morphological modifications of the NRs (Figure S2). NRs are thinner and present more kinks. It is also observed that additional monolayers grow on the sides of the NRs. The VI/III ratio of 4.2 does not show morphological modifications of the NRs. Different growth times have been explored for these growth conditions (550 °C, VI/III: 4.2) and typical dimensions and growth rates are summarized in Table 1 and table presented in Figure S1, respectively.

It is observed that NRs grown under those conditions are narrower than the ones obtained for a VI/III ratio of 5.1. The growth rate is reduced by roughly a factor 1.8 as the VI/III ratio is reduced from 5.1 to 4.2. This could indicate that the GaSe NR growth is limited by "feeding" the catalyst with the Se element. This behavior can be compared to previous works

on Ga-catalyzed VLS growth of GaAs nanowires (GaAs-NWs)[52−54] where As flow drives the NW growth rate and their final length. In the case of GaSe NRs, the growth rate seems to be driven in the same way by the Se flow.

A special attention is now paid to the catalysts and the link between their sizes and the NR width. In our case, the size of the catalysts, at the end of the VLS growth, is always larger than NRs. In Figure S4a, the size of the catalyst is about 430 nm, which is around 30 times larger than the initially formed indium droplets. The NR width is 180 nm. Catalyst sizes at the end of the growth, for different growth conditions, are presented in Table 2. To understand this large discrepancy between the initial size of In droplets and the final size of the catalysts, different assumptions can be made.

The first one is that the size of the In droplets evolves during the temperature ramp-up between the In droplet deposition temperature (400 °C) and the NR growth temperature range (550−620 °C). To check this assumption, the substrate temperature has been raised up to 620 °C, after the In droplet formation, without growing any GaSe NR. No change in size or density of the In droplets was observed in SEM images (Figure S3a).

The second assumption is that the chemical composition of the catalyst evolves during either the initial stages or during the growth of the NRs. To explore this, we have monitored the behavior of the In droplets after ramping-up the temperature and introducing the gallium precursor in the growth chamber for 30 s. SEM images reveal an increase of droplets size (typical diameter: 40 nm), but no modification of the droplets density (Figure S3b). Chemical composition of the droplets is analyzed after the growth of the NRs.

STEM and EDX analysis of the catalyst are presented in Figure S4. This analysis was performed on NRs grown at 620 °C for 1000 s, with a VI/III ratio of 5.1, which were dropcasted on the TEM membrane. The EDX analysis clearly shows that the NRs are composed of Ga and Se. The catalyst presents a gallium-rich core and a shell of gallium−selenium alloy. Indium, which is the initial element of the catalyst is not detected. A small peak of oxygen was observed (the EDX spectrum is shown in Figure S5), which might be related to the surface oxidation after the growth process.

On the basis of these observations, we propose the following model to explain the growth of GaSe NRs (see Figure 3 for a schematic representation of the model). After the formation of indium droplets and the temperature ramp-up to the growth temperature range (550−620 °C), gallium and selenium precursors are introduced into the MOCVD growth chamber. A preferential reaction exists between indium droplets and gallium precursor as In−Ga alloy has a melting point temperature lower than the growth temperature.[55] The gallium precursor is decomposed at the surface of the In droplet, creating a Ga−In alloyed droplet. Selenium precursor might react with this Ga−In droplet but NRs do not start growing until the catalyst reaches a critical size Se atoms then diffuse through the catalyst to the solid−liquid interface to grow a GaSe NR. Colombo et al.[52] proposed a similar mechanism for Ga-assisted GaAs NW VLS growth.

As shown in Figure S4, the chemical composition of the deposited In droplets evolve during the initial stages of growth. The growth of the GaSe NRs occurs *via* Ga-rich catalysts which are always larger than the NRs and both of them increase in size with the growth time, as shown in Table 2. All these observations are consistent with the existing models

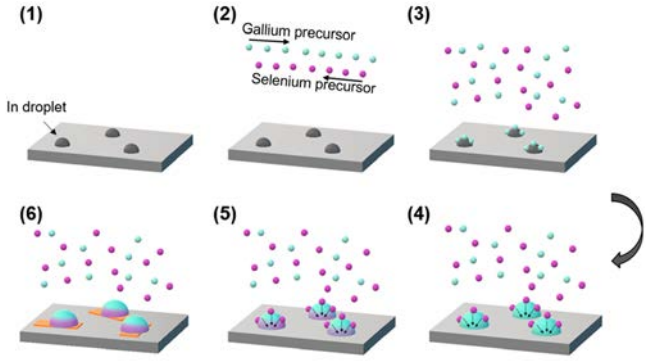

Figure 3. Scheme of the proposed model for the growth of GaSe NRs. Six steps are presented. (1) Indium catalysts are deposited on the SiO_2/Si wafer. (2) Temperature is increased to the growth temperature. Gallium (light blue) and selenium (purple) precursors are introduced in the growth chamber. (3) Gallium reacts with indium catalysts. (4) Selenium precursor reacts with gallium-rich catalysts. (5) Selenium atoms diffuse through gallium-rich catalysts to the liquid/solid interface. (6) Precipitation of GaSe at the liquid/solid interface and GaSe NR growth.

relating to Ga-catalyzed growth of GaAs NWs, which show that the gallium catalysts continue to grow while the gallium precursor is introduced in the chamber.[53,56−58]

At the end of the growth, the precursor flows are stopped and temperature is decreased. In the case of Ga-catalyzed growth of GaAs NWs, As is not detected in the Ga droplet as it desorbs.[59] In our case, we observe selenium alloyed with gallium atoms, at the surface of the catalyst once the system is cooled down. The absence of indium in the catalyst (as shown on the spectrum of Figure S5), can be explained either by a diffusion of indium into the NR during the growth or by desorption of this element. In the case of diffusion, the number of indium atoms, in comparison with the number of gallium and selenium atoms in the NR, would be very small and difficult to quantify.

As previously mentioned, the NR width and catalyst size increase with growth time. The invert-tapering phenomenon could explain this behavior in consistency with our proposed model. In the case of Ga-assisted GaAs NW growth, an invert-tapering phenomenon occurs under a gallium-rich environment and small V/III ratios.[52−54,56,57] When the catalyst is exposed to gallium during the growth, its size increases with growth time. The NW width evolves simultaneously with the size of the catalyst to preserve the same contact angle between the catalyst and the NW. In our study, the growth conditions (small VI/III ratio and gallium-rich catalyst) are favorable to the occurrence of this phenomenon.

To explore the optoelectronic properties of the GaSe NRs, we selected samples with the largest width and thickness to maximize the photodetection. Indeed, in contrast to 2D materials such as TMDCs, which present a direct bandgap for only one monolayer,[26] GaSe presents a direct bandgap for a thickness above two monolayers. For a thickness from 15 monolayers and above, the bandgap of the GaSe remains direct and is fixed around 2 eV.[24] Thus, thicker and wider NRs allow to optimize the optical properties of the NRs. Hence, the GaSe NRs investigated were the sample grown at 620 °C, with a VI/III ratio of 5.1 and growth times ranging between 500 and 1000 s. Figure 4a shows a high-magnification SEM image of a bent NR. The NR width is about 260 nm in length and the

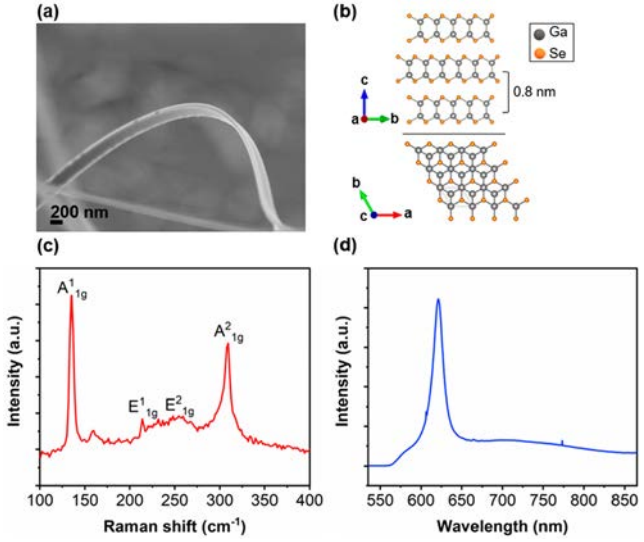

Figure 4. (a) SEM image of a bent NR which is about 260 nm wide and 58 nm thick. (b) Crystal structure of GaSe.[62−69] (c) Raman spectrum of a GaSe NR. (d) Photoluminescence spectrum of a GaSe NR illuminated at 514 nm.

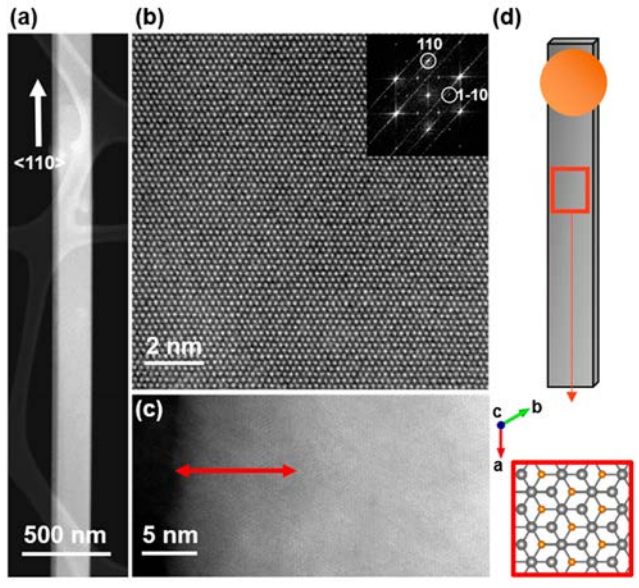

Figure 5. STEM/TEM observations of a GaSe NR (growth parameters: 550 °C, 500 s, VI/III: 4.2). (a) Low-magnification STEM image of a dropcasted NR on TEM grid. (b) HR-STEM image of the well-organized structure of the GaSe at the center of the NR. The diffraction pattern acquired on the image is shown as inset. The measured lattice parameters in the (100) and (110) plans, i.e., 0.320 and 0.191 nm, respectively, are consistent with the hexagonal structure of GaSe. (c) HR-STEM image of the amorphous zone observed at the extreme edge of the NR. The transition area (5−10 nm) from the amorphous zone to the well-organized gallium selenide material is indicated by the red arrow. (d) Schematic representation of the observed zone on the NR. The red square shows the atomic structure observed in panel b where gray and orange balls are Ga and Se atoms, respectively.

observed thickness is about 58 nm, which is equivalent to ∼72 monolayers of GaSe,[60] where a so-called monolayer is composed of a tetra layer structure in the form of X−M−M−X (M = Ga; X = Se). Two monolayers are bonded through van der Waals bonds with an interlayer spacing of 0.8 nm. Figure 4b shows a schematic of the GaSe crystal structure.

The crystal quality of the GaSe NRs was first investigated by Raman spectroscopy measurements performed on GaSe NRs dropcasted on SiO_2/Si substrates. Figure 4c shows the obtained Raman spectrum with four vibration modes at 132, 206, 252, and 307 cm^{-1}, which can be respectively attributed to the tabulated A^1_{1g}, E^1_{2g}, E^2_{1g}, and A^2_{1g} modes of GaSe. The A^1_{1g} and A^2_{1g} modes are attributed to the out-of-plane vibrations, whereas the E^1_{2g} and E^2_{1g} are from in-plane vibrations.[61]

Further investigations on the crystal structure of the NRs were made by STEM characterizations. NRs were observed in both top and cross-section views. Figure 5a shows a typical low-magnification STEM image of a dropcasted NR on a TEM membrane, observed in top-view. The growth direction is along ⟨110⟩. Figure 5b shows HR-STEM image of the well-organized GaSe structure at the center of the NR. No defects are observed and the diffraction pattern indicates the high crystalline quality of the NR. The measured lattice parameter of 0.320 nm is consistent with the (100) plan of the hexagonal structure of GaSe. This observation is consistent with the synthesis of the ε-phase of the GaSe, which is a hexagonal crystal structure from the space group D^1_{3h}.[70] Figure 5c shows an HR-STEM image of the microstructure at the edges of the NRs. An amorphous zone of several nanometers is observed on both sides of the NR. The amorphous zone is observed on several NRs.

Figure 6 shows cross-section STEM view and EDX analysis of a GaSe NR. This observation was possible due to a specific position of the NR on the TEM membrane which allows to observe GaSe layers stacked along the *c*-axis in the NR (Figure 6a) with an interlayer spacing of 0.8 nm consistent with the literature data.[60] Above and below the well-crystalline GaSe layers, an amorphous layer of 5−6 nm is again observed. EDX analyses (Figure 6) reveal that the crystalline layers of the NR are composed of Ga and Se elements, whereas only Ga and O elements are identified in the amorphous areas (Se is not detected). Observation of this amorphous zone simultaneously on the edge (Figure 5c) and above and below the crystalline layers (Figure 6a) of the NRs, is consistent with the presence of a shell of native gallium oxide GaO_x covering the NRs. GaSe is known to be highly reactive with the air and to form a native oxide.[71,72] The NRs were not stocked under any peculiar atmosphere, which explains the observation of this oxide shell formation.

The morphology and structural quality of the GaSe NRs have been investigated by SEM, Raman spectroscopy, and STEM-EDX characterizations. The morphology of the NRs has been monitored by statistical SEM measurements. We have shown that we synthesized straight NRs with a variable width in a range of a hundred of nanometers and a length of several tenths of micrometers. The Raman spectroscopy coupled with STEM-EDX characterizations have shown that the NRs were indeed composed by GaSe crystalline layers in the core of the NRs. The monocrystalline quality of the GaSe layers has been investigated by STEM and we have shown that we synthesized the ε-phase of the GaSe, which is a hexagonal crystal structure from the space group D^1_{3h}. Furthermore, an amorphous zone has been observed, by STEM, on the edge of NRs and above and under the crystalline layers. The EDX analysis has shown that the crystalline GaSe layers were encapsulated by a native oxide shell of GaOx.

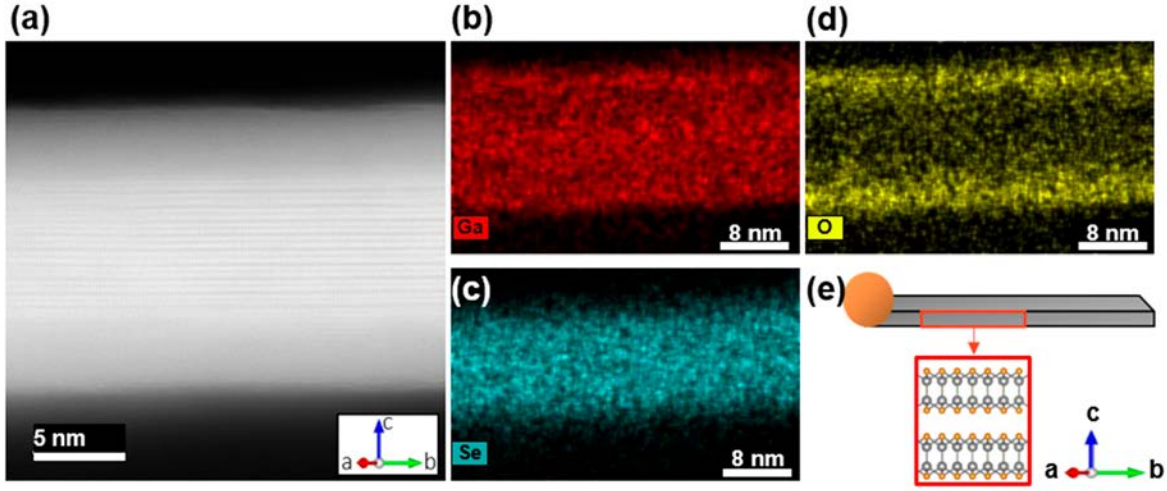

Figure 6. STEM/EDX observations of a GaSe NR in a cross-section view (growth parameters: 550 °C, 500 s, VI/III: 4.2). (a) STEM observation. (b–d) EDX analysis and element identification of (b) gallium, (c) selenium, and (d) oxygen. (e) Schematic of the observed zone. The red square shows the atomic structure observed in panel a where gray and orange balls are Ga and Se atoms, respectively.

Complementary to the crystal structure characterizations, optical properties of the NRs were then characterized by photoluminescence analyses with a 514 nm laser, focused on several NRs. Different samples have been analyzed, NRs on their growth substrates and NRs dispersed on SiO_2/Si or Si_3N_4/SiO_2/Si substrates. All the analyzed NRs are multilayers NRs. In these three cases, we observed a photoluminescence peak around 2 eV, which is consistent for thick NRs (with a number of monolayers above 15).[24] Thus, the bandgap energy of the studied NRs is consistent with the one obtained for bulk GaSe.[73] Figure 4d shows the photoluminescence response peak acquired on a NR.

Electrical transport properties and photoresponse behavior of the GaSe NRs were then investigated using the fabricated test structures (see Experimental Section). Figure 7a shows an SEM image of one of the test structures where the electrodes are colored in yellow and GaSe NR is colored in blue. A cross-section TEM image of the GaSe NR with the Ni/Au metal contact on top is presented in Figure 7b. An amorphous region around the NR is observed, consistent with Figures 5c and 6a. It should be noted that the NRs were grown about 5 months before the fabrication of the devices. Assuming this amorphous layer to be gallium oxide (see Figure 6), the width and height of the original NR are ~270 nm and ~60 nm, which are consistent with growth conditions at 620 °C, 1000 s, and VI/III ratio of 5.1 (see Table 1). The central region of the NR confirms the crystalline structure of the NR as discussed in the previous section (Figures 5 and 6). Current versus voltage (I–V) characteristics of the two-terminal device using contacts C1 and C2 at different temperatures measured in the dark and under microscope white light illumination are shown in Figure 7c in linear scale and in Figure 7d in semilog scale. The measured current level at 25 °C, under white light, is about a tenth of pA which is about two to three decades lower than the measured current level for other GaSe NRs.[38,40] The relatively low current levels (in the pA range) are consistent with a range of factors such as the GaSe bandgap of around 2 eV (see PL response, Figure 4d), no intentional doping during the growth and almost defect-free GaSe material. These factors are all expected to lead to a large band offset at the metal–GaSe interface. In addition, the presence of the amorphous oxide region around the NRs creates a barrier for carrier transport, to and from the GaSe NR, at the interface with the metallic contacts.

When the structure is illuminated, current increases and a symmetric IV response is obtained, as shown in Figure 7d, consistent with photogenerated carriers reducing the GaSe NR resistance, resulting in the applied voltage dropping primarily across the contact regions of the back-to-back Schottky diode (BtB-SD) structure.[74] It is noted that the contact region is comprised of a Ni/Ga oxide/GaSe structure and not a direct contact of the metal to the GaSe. To evaluate the hypothesis of a BtB-SD, I–V data at 100 °C, as an example, is fitted using the BtB-SD equation. The form of the experimental response does match the BtB-SD model (see Figure 7c); however, the rate of change of current with applied voltage prior to current saturation requires a large effective ideality factor. The large deviation from ideality can be explained based on the presence of a series resistance included in the BtB-SD configuration. As recently demonstrated in the literature,[75] the incorporation of a series resistance in the analysis of the BtB-SD structure results in large effective ideality factors. In our case, the origin of the series resistance is consistent with the amorphous Ga oxide region between the GaSe and the metallic contacts as observed in the TEM analysis (see Figure 8b).

The hyperbolic sine function of the BtB-SD equation results in a linear increase in current at low fields, which is also observed in our GaSe NR devices, as can be seen in Figure S6. The conduction in this region of the IV response is thermally activated with the activation energy of 0.22 eV at 3 V. These results indicate a need to remove the native oxide in the GaSe immediately prior to metal deposition. For voltages beyond ±10 V, the current deviates from being completely flat and shows an increasing trend as the electric field increases (see Figure 7d). Within this region, the current is proportional to $V^{1/4}$ consistent with field-induced barrier lowering.[74] To further investigate this effect, we have extracted the activation energy of 0.23 and 0.2 eV at 9 and 20 V, respectively, using the Arrhenius plot of current versus q/k_BT, showing consistency with the field-induced barrier lowering. It is anticipated that at higher temperatures, the conductivity of Ga oxide increases and hence a larger fraction of the applied voltage drops across

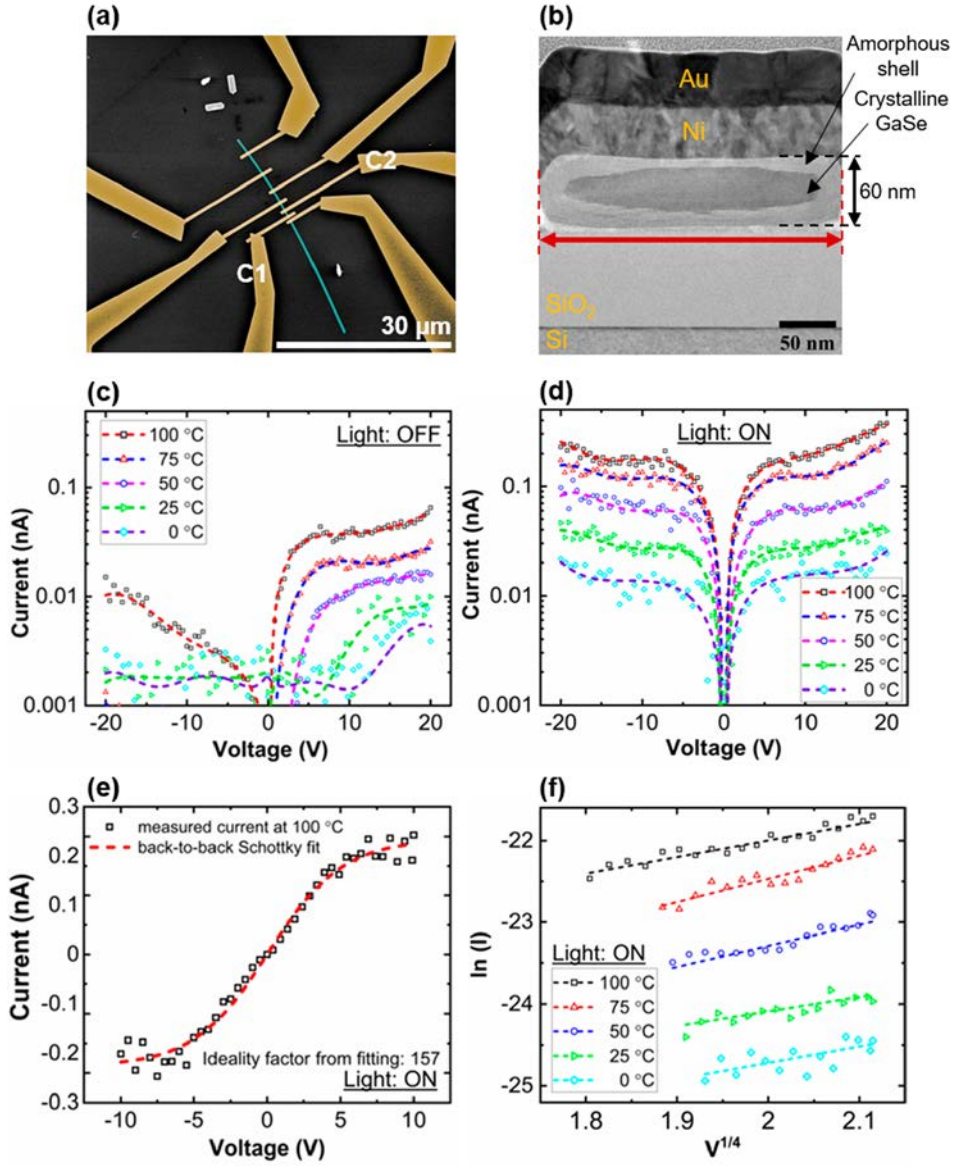

Figure 7. (a) SEM image of GaSe NR device with electrodes colored in yellow and NR in blue. (b) Cross-sectional TEM image of a GaSe NR with Ni/Au metal contact on top. The amorphous region around the highly crystalline GaSe NR in the middle is Ga oxide (see Figure 6). $I-V$ characteristic of a GaSe NR measured at different temperatures from 0 to 100 °C (c) in the dark and (d) under microscope white light illumination. (e) $I-V$ curve fitted with back-to-back Schottky barrier equation with ideality factor as a variable. (f) Ln(I) vs $V^{1/4}$ demonstrating field-induced barrier lowering.

the barriers. As a result, it is expected that the current deviation from saturation to ln(I) proportional to $V^{1/4}$ should shift to lower voltages as temperature increases. This is observed experimentally as shown in Figure 7f.

A stable and repeatable operation of dynamic photoresponse was observed for the GaSe NR under illumination. As can be seen in Figure 8a, with light illumination OFF and ON, the current exhibited a level of ~4 and 70 pA, respectively, demonstrating an I_{ON}/I_{OFF} ratio of about 17 at 25 °C and under V_{bias} = 20 V, which is two[38] to five[40] decades lower than precedent works. Figure 8b shows the variation of I_{ON} and I_{OFF} with temperature, where the I_{ON}/I_{OFF} ratio ($Y2$-axis) displays a reduction with increasing temperature. Further details of the photoresponse of the GaSe NR at various temperatures are presented in Figure S7. It is noted that after the first illumination pulse, the OFF current of the subsequent pulses plateaus at a level marginally higher than the very first pulse. This could be an indication of charges being captured in trap states and requires future study. To further investigate the rise and decay time constants of the photoresponse, we have fitted the response once the light is switched ON using a single exponential equation with a rise time constant of t_r: $y = y_0 + A_1 e^{-(x-x_0)/t_r}$. As can be seen in Figure 8c, the rise time of t_r = 0.156 s has been obtained at room temperature. When the light is switched OFF, two regimes can be observed in the response, a sharp decrease followed by a slow decay time. Hence, to extract the decay time we have fitted the data using the following equation with two exponential terms with decay time constants of t_{d1} and t_{d2}: $y = y_0 + A_1 e^{-(x - x_0)/t_{d1}} + A_2 e^{-(x-x_0)/t_{d2}}$. The decay time constants of t_{d1} = 0.118 s and t_{d2} = 2.025 s have been obtained, as shown in Figure 8d. Both rise and decay

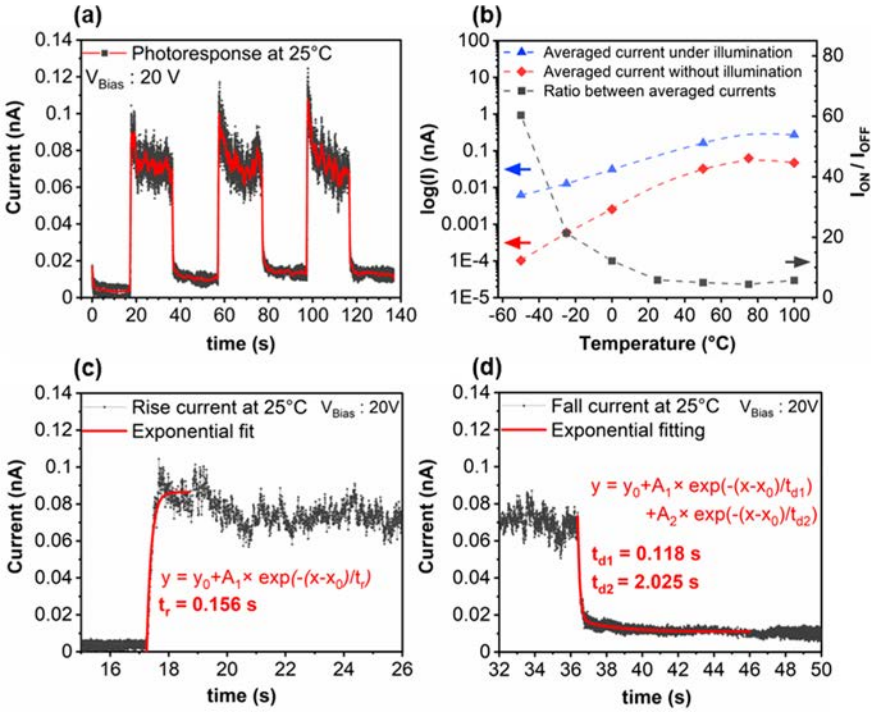

Figure 8. (a) Photoresponse of GaSe NR using microscope white light at 25 °C. (b) Absolute values of the illuminated (light ON) and dark (light OFF) current levels versus the temperature. The second *Y*-axis (*Y*2-axis) displays the ratio of the current with the light ON to the current when the light OFF. (c, d) Measured and fitted curves to extract the (c) rise and (d) decay times of the photoresponse at 25 °C.

time constants are in good agreement with the reported literature.[40,43]

CONCLUSION

In conclusion, we demonstrated the growth of GaSe NRs directly on 300 mm SiO_2/Si substrates by MOCVD. NRs are grown via a VLS method using indium droplets as catalysts to initiate the growth. We explored the impact of growth temperature, growth time, and VI/III ratio on the morphology of the GaSe NRs and on the evolution of the catalysts. On the basis of these results, a detailed model was proposed to explain the different stages of the GaSe NR growth. The crystalline quality of the core of the NRs was demonstrated by Raman spectroscopy and HR-STEM analyses. An amorphous shell was observed around the crystalline GaSe layers and was identified as gallium oxide by EDX. NR-based devices were fabricated followed by temperature-dependent electrical characterization with and without microscope white light illumination. The electrical results were fitted with the back-to-back Schottky diode model, revealing large deviation from ideal interface consistent with the presence of the amorphous gallium oxide region between the crystalline GaSe NR and the metal contact. A stable and repeatable operation of dynamic photoresponse was achieved on a single GaSe NR with an ON/OFF current ratio of 17 at room temperature.

ASSOCIATED CONTENT

Supporting Information

The Supporting Information is available free of charge at https://pubs.acs.org/doi/10.1021/acsanm.1c01141.

Table presenting the average growth rates for NRs grow at 600 and 550 °C; SEM images of NRs grown at 620 °C for 1000 s with a VI/III ratio of 5.9; SEM images of In droplets after a temperature ramp-up and the introduction of the gallium precursor; SEM image and STEM-EDX analysis of a droplet at the tip of an NR; EDX spectrum of a catalyst at the end of an NR; *I*−*V* plot showing the linear behavior of the curves for voltages between 0 and 4 V; photoresponse plots at temperature between 25 and 100 °C; SEM image of a contacted NR with labeled electrodes; photoresponse plots for 50, 75, and 100 °C for different contacts gaps; *I*−*V* plots measured at 50, 75, and 100 °C in the dark and under illumination for different contacts gaps; behavior of current measured for light ON and of the ratio ION/IOFF in function of contacts gaps length (PDF)

AUTHOR INFORMATION

Corresponding Author

Thierry Baron − *Université Grenoble Alpes, CNRS, CEA/LETI Minatec, Grenoble INP, LTM, Grenoble Cedex F-38054, France;* orcid.org/0000-0001-5005-6596; Email: thierry.baron@cea.fr

Authors

Pauline Hauchecorne − *Université Grenoble Alpes, CNRS, CEA/LETI Minatec, Grenoble INP, LTM, Grenoble Cedex F-38054, France; Université Grenoble Alpes, Grenoble F-38000, France; CEA-LETI, Université Grenoble Alpes, Grenoble F-38054, France*

Farzan Gity − *Tyndall National Institute, University College Cork, Cork T12 R5CP, Ireland;* orcid.org/0000-0003-3128-1426

Mickael Martin − *Université Grenoble Alpes, CNRS, CEA/LETI Minatec, Grenoble INP, LTM, Grenoble Cedex F-38054, France*

Hanako Okuno − *CEA, IRIG-MEM, Université Grenoble Alpes, Grenoble 38000, France*
Shubhadeep Bhattacharjee − *Tyndall National Institute, University College Cork, Cork T12 R5CP, Ireland; Department of Physics, University of Manchester, Manchester M139PL, United Kingdom;* orcid.org/0000-0002-5813-033X
Jérémy Moeyaert − *Université Grenoble Alpes, CNRS, CEA/LETI Minatec, Grenoble INP, LTM, Grenoble Cedex F-38054, France*
Denis Rouchon − *CEA-LETI, Université Grenoble Alpes, Grenoble F-38054, France*
Bérangère Hyot − *CEA-LETI, Université Grenoble Alpes, Grenoble F-38054, France*
Paul K. Hurley − *Tyndall National Institute, University College Cork, Cork T12 R5CP, Ireland*

Notes

The authors declare no competing financial interest.

ACKNOWLEDGMENTS

This work was partly supported by the French RENATECH network, and by the French National Research Agency in the framework of the Investissements d'Avenir program (ANR-15-IDEX-02). The authors from the Tyndall National Institute acknowledge the financial support of Science Foundation Ireland (AMBER 12/RC/2278 P2).

REFERENCES

(1) Shi, L.; Nihtianov, S. Comparative Study of Silicon-Based Ultraviolet Photodetectors. *IEEE Sens. J.* **2012**, *12* (7), 2453−2459.
(2) Sang, L.; Liao, M.; Sumiya, M. A Comprehensive Review of Semiconductor Ultraviolet Photodetectors: From Thin Film to One-Dimensional Nanostructures. *Sensors* **2013**, *13* (8), 10482−10518.
(3) Yu, J.; Shan, C. X.; Huang, X. M.; Zhang, X. W.; Wang, S. P.; Shen, D. Z. ZnO-Based Ultraviolet Avalanche Photodetectors. *J. Phys. D: Appl. Phys.* **2013**, *46* (30), 305105.
(4) Fortier, S. M.; Hammarstrom, J. H.; Ryker, S. J.; Day, W. C.; Seal, R. R. *USGS Critical Minerals Review*; U.S. Geological Survey: Washington, D.C., 2018, 16.
(5) Hayes, S. M.; McCullough, E. A. Critical Minerals: A Review of Elemental Trends in Comprehensive Criticality Studies. *Resour. Policy* **2018**, *59*, 192−199.
(6) European Commission. *Report on Critical Raw Materials for the EU−Critical Raw Materials Profiles*; Ares(2015)1819595 ; European Commission: Brussels, Belgium, 2015.
(7) *Critical Metals Handbook*; Gunn, G., Ed.; John Wiley & Sons: Hoboken, NJ, 2014.
(8) European Commission. *Résilience Des Matières Premières Critiques: La Voie à Suivre Pour Un Renforcement de La Sécurité et de La Durabilité*; Communication de la Commission au Parlement Européen, au Conseil, au Comité Economique et Social Européen et au Comité des Régions; COM, 2020; Vol. *474*.
(9) *Mineral Commodity Summaries 2020*; U.S. Geological Survey: Washington, D.C., 2020; p 200.
(10) Lan, C.; Shi, Z.; Cao, R.; Li, C.; Zhang, H. 2D Materials beyond Graphene toward Si Integrated Infrared Optoelectronic Devices. *Nanoscale* **2020**, *12* (22), 11784−11807.
(11) Guan, X.; Yu, X.; Periyanagounder, D.; Benzigar, M. R.; Huang, J.; Lin, C.; Kim, J.; Singh, S.; Hu, L.; Liu, G.; Li, D.; He, J.; Yan, F.; Wang, Q. J.; Wu, T. Recent Progress in Short- to Long-Wave Infrared Photodetection Using 2D Materials and Heterostructures. *Adv. Opt. Mater.* **2021**, *9* (4), 2001708.
(12) Wasala, M.; Sirikumara, H. I.; Raj Sapkota, Y.; Hofer, S.; Mazumdar, D.; Jayasekera, T.; Talapatra, S. Recent Advances in Investigations of the Electronic and Optoelectronic Properties of Group III, IV, and V Selenide Based Binary Layered Compounds. *J. Mater. Chem. C* **2017**, *5* (43), 11214−11225.
(13) Yang, Z.; Hao, J. Recent Progress in 2D Layered III-VI Semiconductors and Their Heterostructures for Optoelectronic Device Applications. *Adv. Mater. Technol.* **2019**, *4* (8), 1900108.
(14) Gao, L.; Ma, C.; Wei, S.; Kuklin, A. V.; Zhang, H.; Ågren, H. Applications of Few-Layer Nb $_2$ C MXene: Narrow-Band Photodetectors and Femtosecond Mode-Locked Fiber Lasers. *ACS Nano* **2021**, *15* (1), 954−965.
(15) He, J.; Tao, L.; Zhang, H.; Zhou, B.; Li, J. Emerging 2D Materials beyond Graphene for Ultrashort Pulse Generation in Fiber Lasers. *Nanoscale* **2019**, *11* (6), 2577−2593.
(16) Tuo, M.; Xu, C.; Mu, H.; Bao, X.; Wang, Y.; Xiao, S.; Ma, W.; Li, L.; Tang, D.; Zhang, H.; Premaratne, M.; Sun, B.; Cheng, H.-M.; Li, S.; Ren, W.; Bao, Q. Ultrathin 2D Transition Metal Carbides for Ultrafast Pulsed Fiber Lasers. *ACS Photonics* **2018**, *5* (5), 1808−1816.
(17) Fortin, E.; Sears, W. M. Photovoltaic Effect and Optical Absorption in MoS2. *J. Phys. Chem. Solids* **1982**, *43* (9), 881−884.
(18) Dhanabalan, S. C.; Ponraj, J. S.; Zhang, H.; Bao, Q. Present Perspectives of Broadband Photodetectors Based on Nanobelts, Nanoribbons, Nanosheets and the Emerging 2D Materials. *Nanoscale* **2016**, *8* (12), 6410−6434.
(19) Lou, Z.; Liang, Z.; Shen, G. Photodetectors Based on Two Dimensional Materials. *J. Semicond.* **2016**, *37* (9), 091001.
(20) Han, P.; St. Marie, L.; Wang, Q. X; Quirk, N.; El Fatimy, A.; Ishigami, M.; Barbara, P. Highly Sensitive MoS $_2$ Photodetectors with Graphene Contacts. *Nanotechnology* **2018**, *29* (20), 20LT01.
(21) Wang, Q.; Lai, J.; Sun, D. Review of Photo Response in Semiconductor Transition Metal Dichalcogenides Based Photosensitive Devices. *Opt. Mater. Express* **2016**, *6* (7), 2313.
(22) Hu, P.; Wen, Z.; Wang, L.; Tan, P.; Xiao, K. Synthesis of Few-Layer GaSe Nanosheets for High Performance Photodetectors. *ACS Nano* **2012**, *6* (7), 5988−5994.
(23) Ko, P. J.; Abderrahmane, A.; Takamura, T.; Kim, N.-H.; Sandhu, A. Thickness Dependence on the Optoelectronic Properties of Multilayered GaSe Based Photodetector. *Nanotechnology* **2016**, *27* (32), 325202.
(24) Terry, D. J.; Zólyomi, V.; Hamer, M.; Tyurnina, A. V.; Hopkinson, D. G.; Rakowski, A. M.; Magorrian, S. J.; Clark, N.; Andreev, Y. M.; Kazakova, O.; Novoselov, K.; Haigh, S. J.; Fal'ko, I.; Gorbachev, R. Infrared-to-Violet Tunable Optical Activity in Atomic Films of GaSe, InSe, and Their Heterostructures. *2D Mater.* **2018**, *5* (4), 041009.
(25) Nizametdinova, M. A. The Reflection Spectrum of GaSe and GaS Single Crystals near the Fundamental Absorption Edge. *Phys. Status Solidi B* **1967**, *19* (2), K111−K112.
(26) Wang, G.; Chernikov, A.; Glazov, M. M.; Heinz, T. F.; Marie, X.; Amand, T.; Urbaszek, B. *Colloquium*: Excitons in Atomically Thin Transition Metal Dichalcogenides. *Rev. Mod. Phys.* **2018**, *90* (2), 021001.
(27) Lei, S.; Ge, L.; Liu, Z.; Najmaei, S.; Shi, G.; You, G.; Lou, J.; Vajtai, R.; Ajayan, P. M. Synthesis and Photoresponse of Large GaSe Atomic Layers. *Nano Lett.* **2013**, *13* (6), 2777−2781.
(28) Zhou, Y.; Nie, Y.; Liu, Y.; Yan, K.; Hong, J.; Jin, C.; Zhou, Y.; Yin, J.; Liu, Z.; Peng, H. Epitaxy and Photoresponse of Two-Dimensional GaSe Crystals on Flexible Transparent Mica Sheets. *ACS Nano* **2014**, *8* (2), 1485−1490.
(29) Huang, H.; Wang, P.; Gao, Y.; Wang, X.; Lin, T.; Wang, J.; Liao, L.; Sun, J.; Meng, X.; Huang, Z.; Chen, X.; Chu, J. Highly Sensitive Phototransistor Based on GaSe Nanosheets. *Appl. Phys. Lett.* **2015**, *107* (14), 143112.
(30) Cao, Y.; Cai, K.; Hu, P.; Zhao, L.; Yan, T.; Luo, W.; Zhang, X.; Wu, X.; Wang, K.; Zheng, H. Strong Enhancement of Photoresponsivity with Shrinking the Electrodes Spacing in Few Layer GaSe Photodetectors. *Sci. Rep.* **2015**, *5* (1), 8130.

(31) Yuan, X.; Tang, L.; Liu, S.; Wang, P.; Chen, Z.; Zhang, C.; Liu, Y.; Wang, W.; Zou, Y.; Liu, C.; Guo, N.; Zou, J.; Zhou, P.; Hu, W.; Xiu, F. Arrayed van Der Waals Vertical Heterostructures Based on 2D GaSe Grown by Molecular Beam Epitaxy. *Nano Lett.* **2015**, *15* (5), 3571−3577.
(32) Curreli, N.; Serri, M.; Zappia, M. I.; Spirito, D.; Bianca, G.; Buha, J.; Najafi, L.; Sofer, Z.; Krahne, R.; Pellegrini, V.; Bonaccorso, F. Liquid-Phase Exfoliated Gallium Selenide for Light-Driven Thin-Film Transistors. *Adv. Electron. Mater.* **2021**, *7* (3), 2001080.
(33) Sorifi, S.; Moun, M.; Kaushik, S.; Singh, R. High-Temperature Performance of a GaSe Nanosheet-Based Broadband Photodetector. *ACS Appl. Electron. Mater.* **2020**, *2* (3), 670−676.
(34) Tan, L.; Liu, Q.; Ding, Y.; Lin, X.; Hu, W.; Cai, M.-Q.; Zhou, H. Effective Shape-Controlled Synthesis of Gallium Selenide Nanosheets by Vapor Phase Deposition. *Nano Res.* **2020**, *13* (2), 557−563.
(35) Peng, H.; Meister, S.; Chan, C. K.; Zhang, X. F.; Cui, Y. Morphology Control of Layer-Structured Gallium Selenide Nanowires. *Nano Lett.* **2007**, *7* (1), 199.
(36) Panda, S. K.; Datta, A.; Sinha, G.; Chaudhuri, S.; Chavan, P. G.; Patil, S. S.; More, M. A.; Joag, D. S. Synthesis of Well-Crystalline GaS Nanobelts and Their Unique Field Emission Behavior. *J. Phys. Chem. C* **2008**, *112* (16), 6240−6244.
(37) Shen, G.; Chen, D.; Chen, P.-C.; Zhou, C. Vapor-Solid Growth of One- Dimensional Layer-Structured Gallium Sulfide Nanostructures. *ACS Nano* **2009**, *3* (5), 1115−1120.
(38) Xiong, X.; Zhang, Q.; Zhou, X.; Jin, B.; Li, H.; Zhai, T. One-Step Synthesis of p-Type GaSe Nanoribbons and Their Excellent Performance in Photodetectors and Phototransistors. *J. Mater. Chem. C* **2016**, *4* (33), 7817−7823.
(39) Jung, C. S.; Park, K.; Shojaei, F.; Oh, J. Y.; Im, H. S.; Lee, J. A.; Jang, D. M.; Park, J.; Myoung, N.; Lee, C.-L.; Lee, J. W.; Song, J. K.; Kang, H. S. Photoluminescence and Photocurrents of $GaS_{1-x}Se_x$ Nanobelts. *Chem. Mater.* **2016**, *28* (16), 5811−5820.
(40) Tang, L.; Zhao, Z.; Yuan, S.; Yang, T.; Zhou, B.; Zhou, H. Self-Catalytic VLS Growth One Dimensional Layered GaSe Nanobelts for High Performance Photodetectors. *J. Phys. Chem. Solids* **2018**, *118*, 186−191.
(41) Li, S.; Lin, Y.-C.; Zhao, W.; Wu, J.; Wang, Z.; Hu, Z.; Shen, Y.; Tang, D.-M.; Wang, J.; Zhang, Q.; Zhu, H.; Chu, L.; Zhao, W.; Liu, C.; Sun, Z.; Taniguchi, T.; Osada, M.; Chen, W.; Xu, Q.-H.; Wee, A. T. S.; Suenaga, K.; Ding, F.; Eda, G. Vapour-Liquid-Solid Growth of Monolayer MoS2 Nanoribbons. *Nat. Mater.* **2018**, *17* (6), 535−542.
(42) Liao, F.; Wang, Y.; Peng, T.; Peng, J.; Gu, Z.; Yu, H.; Chen, T.; Yu, J.; Gu, F. Highly Efficient Nonlinear Optical Conversion in Waveguiding GaSe Nanoribbons with Pump Pulses Down to a Femto-Joule Level. *Adv. Opt. Mater.* **2018**, *6* (5), 1701012.
(43) Wu, C.-Y.; Zhu, H.; Wang, M.; Kang, J.; Xie, C.; Wang, L.; Luo, L.-B. Controlled Synthesis of GaSe Microbelts for High-Gain Photodetectors Induced by the Electron Trapping Effect. *J. Mater. Chem. C* **2020**, *8*, 5375−5379.
(44) Sutter, E.; French, J. S.; Sutter, S.; Idrobo, J. C.; Sutter, P. Vapor-Liquid-Solid Growth and Optoelectronics of Gallium Sulfide van Der Waals Nanowires. *ACS Nano* **2020**, *14*, 6117−6126.
(45) Xu, J.; Li, H.; Fang, S.; Jiang, K.; Yao, H.; Fang, F.; Chen, F.; Wang, Y.; Shi, Y. Synthesis of Bismuth Sulfide Nanobelts for High Performance Broadband Photodetectors. *J. Mater. Chem. C* **2020**, *8* (6), 2102−2108.
(46) Chowdhury, T.; Kim, J.; Sadler, E. C.; Li, C.; Lee, S. W.; Jo, K.; Xu, W.; Gracias, D. H.; Drichko, N. V.; Jariwala, D.; Brintlinger, T. H.; Mueller, T.; Park, H.-G.; Kempa, T. J. Substrate-Directed Synthesis of MoS2 Nanocrystals with Tunable Dimensionality and Optical Properties. *Nat. Nanotechnol.* **2020**, *15* (1), 29−34.
(47) Aljarb, A.; Fu, J.-H.; Hsu, C.-C.; Chuu, C.-P.; Wan, Y.; Hakami, M.; Naphade, D. R.; Yengel, E.; Lee, C.-J.; Brems, S.; Chen, T.-A.; Li, M.-Y.; Bae, S.-H.; Hsu, W.-T.; Cao, Z.; Albaridy, R.; Lopatin, S.; Chang, W.-H.; Anthopoulos, T. D.; Kim, J.; Li, L.-J.; Tung, V. Ledge-Directed Epitaxy of Continuously Self-Aligned Single-Crystalline Nanoribbons of Transition Metal Dichalcogenides. *Nat. Mater.* **2020**, *19* (12), 1300−1306.
(48) Sutter, P.; French, J. S.; Khosravi Khorashad, L.; Argyropoulos, C.; Sutter, E. Optoelectronics and Nanophotonics of Vapor-Liquid-Solid Grown GaSe van Der Waals Nanoribbons. *Nano Lett.* **2021**, *21* (10), 4335−4342.
(49) Hao, S.; Yan, S.; Wang, Y.; Xu, T.; Zhang, H.; Cong, X.; Li, L.; Liu, X.; Cao, T.; Gao, A.; Zhang, L.; Jia, L.; Long, M.; Hu, W.; Wang, X.; Tan, P.; Sun, L.; Cui, X.; Liang, S.; Miao, F. Edge-Epitaxial Growth of InSe Nanowires toward High-Performance Photodetectors. *Small* **2020**, *16* (4), 1905902.
(50) Bin, Y.; Xuhui, S.; Sanghyun, J.; Janes, D. B.; Meyyappan, M. Chalcogenide-Nanowire-Based Phase Change Memory. *IEEE Trans. Nanotechnol.* **2008**, *7* (4), 496−502.
(51) Peng, H.; Schoen, D. T.; Meister, S.; Zhang, X. F.; Cui, Y. Synthesis and Phase Transformation of In_2Se_3 and $CuInSe_2$ Nanowires. *J. Am. Chem. Soc.* **2007**, *129* (1), 34−35.
(52) Colombo, C.; Spirkoska, D.; Frimmer, M.; Abstreiter, G.; Fontcuberta i Morral, A. Ga-Assisted Catalyst-Free Growth Mechanism of GaAs Nanowires by Molecular Beam Epitaxy. *Phys. Rev. B: Condens. Matter Mater. Phys.* **2008**, *77* (15), 155326.
(53) Rieger, T.; Heiderich, S.; Lenk, S.; Lepsa, M. I.; Grützmacher, D. Ga-Assisted MBE Growth of GaAs Nanowires Using Thin HSQ Layer. *J. Cryst. Growth* **2012**, *353* (1), 39−46.
(54) Paek, J. H.; Nishiwaki, T.; Yamaguchi, M.; Sawaki, N. Catalyst Free MBE-VLS Growth of GaAs Nanowires on (111)Si Substrate. *Phys. Status Solidi C* **2009**, *6* (6), 1436−1440.
(55) Anderson, T. J.; Ansara, I. The Ga-In (Gallium-Indium) System. *J. Phase Equilib.* **1991**, *12* (1), 64−72.
(56) Tersoff, J. Stable Self-Catalyzed Growth of III-V Nanowires. *Nano Lett.* **2015**, *15*, 6609−6613.
(57) Krogstrup, P.; Jørgensen, H. I.; Johnson, E.; Madsen, M. H.; Sørensen, C. B.; Morral, A. F. i; Aagesen, M.; Nygård, J.; Glas, F. Advances in the Theory of III-V Nanowire Growth Dynamics. *J. Phys. D: Appl. Phys.* **2013**, *46* (31), 313001.
(58) Gibson, S.; LaPierre, R. Study of Radial Growth in Patterned Self-Catalyzed GaAs Nanowire Arrays by Gas Source Molecular Beam Epitaxy: Study of Radial Growth in Patterned Self-Catalyzed GaAs Nanowire Arrays by Gas Source Molecular Beam Epitaxy. *Phys. Status Solidi RRL* **2013**, *7* (10), 845−849.
(59) Morral, A. F. i. Gold-Free GaAs Nanowire Synthesis and Optical Properties. *IEEE J. Sel. Top. Quantum Electron.* **2011**, *17* (4), 819−828.
(60) Kuhn, A.; Chevy, A.; Chevalier, R. Crystal Structure and Interatomic Distances in GaSe. *Phys. Stat. Sol. (a)* **1975**, *31* (2), 469−475.
(61) Hoff, R. M.; Irwin, J. C.; Lieth, R. M. A. Raman Scattering in GaSe. *Can. J. Phys.* **1975**, *53* (17), 1606−1614.
(62) Momma, K.; Izumi, F. VESTA 3 for Three-Dimensional Visualization of Crystal, Volumetric and Morphology Data; *J. Appl. Crystallogr.* **2011**, *44*, 1272−1276.
(63) Downs, R. T.; Hall-Wallace, M. The American Mineralogist Crystal Structure Database. *Am. Mineral.* **2003**, *88*, 247−250.
(64) Gražulis, S.; Chateigner, D.; Downs, R. T.; Yokochi, A. F. T. Crystallography Open Database−an Open-Access Collection of Crystal Structures. *J. Appl. Crystallogr.* **2009**, *42*, 726−729.
(65) Grazulis, S.; Merkys, A.; Vaitkus, A.; Okulic-Kazarinas, M. Computing Stoichiometric Molecular Composition from Crystal Structures. *J. Appl. Crystallogr.* **2015**, *48*, 85.
(66) Gražulis, S.; Daškevič, A.; Merkys, A.; Chateigner, D.; Lutterotti, L.; Quirós, M.; Serebryanaya, N. R.; Moeck, P.; Downs, R. T.; Le Bail, A. Crystallography Open Database (COD): An Open-Access Collection of Crystal Structures and Platform for World-Wide Collaboration. *Nucleic Acids Res.* **2012**, *40* (D1), D420−D427.
(67) Merkys, A.; Vaitkus, A.; Butkus, J.; Okulič-Kazarinas, M.; Kairys, V.; Gražulis, S. COD::CIF::Parser: An Error-Correcting CIF Parser for the Perl Language. *J. Appl. Crystallogr.* **2016**, *49*, 10.
(68) Quiros, M.; Grazulis, S.; Girdzijauskaite, S.; Merkys, A.; Vaitkus, A. Using SMILES Strings for the Description of Chemical Connectivity in the Crystallography Open Database. *J. Cheminf.* **2018**, *10*, 17.

(69) Vaitkus, A.; Merkys, A.; Gražulis, S. Validation of the Crystallography Open Database Using the Crystallographic Information Framework. *J. Appl. Crystallogr.* **2021**, *54*, 661.
(70) Huang, W.; Gan, L.; Li, H.; Ma, Y.; Zhai, T. 2D Layered Group IIIA Metal Chalcogenides: Synthesis, Properties and Applications in Electronics and Optoelectronics. *CrystEngComm* **2016**, *18* (22), 3968−3984.
(71) Rahaman, M.; Rodriguez, R. D.; Monecke, M.; Lopez-Rivera, S. A.; Zahn, D. R. T. GaSe Oxidation in Air: From Bulk to Monolayers. *Semicond. Sci. Technol.* **2017**, *32* (10), 105004.
(72) Kowalski, B. M.; Manz, N.; Bethke, D.; Shaner, E. A.; Serov, A.; Kalugin, N. G. Role of Humidity in Oxidation of Ultrathin GaSe. *Mater. Res. Express* **2019**, *6* (8), 085907.
(73) Voitchovsky, J. P.; Mercier, A. Photoluminescence OfGaSe. *Nuov Cim B* **1974**, *22* (2), 273−292.
(74) Mikhelashvili, V.; Padmanabhan, R.; Eisenstein, G. Simplified Parameter Extraction Method for Single and Back-to-Back Schottky Diodes Fabricated on Silicon-on-Insulator Substrates. *J. Appl. Phys.* **2017**, *122* (3), 034503.
(75) Wang, Z.; Zang, W.; Shi, Y.; Zhu, X.; Rao, G.; Wang, Y.; Chu, J.; Gong, C.; Gao, X.; Sun, H.; Huanglong, S.; Yang, D.; Wangyang, P. Extraction and Analysis of the Characteristic Parameters in Back-to-Back Connected Asymmetric Schottky Diode. *Phys. Status Solidi A* **2020**, *217* (8), 1901018.